Electrochimica Acta 537 (2025) 146903

Contents lists available at ScienceDirect

Electrochimica Acta

journal homepage: www.journals.elsevier.com/electrochimica-acta

Use of DMSO as a co-solvent for aqueous lithium-ion batteries

Ivan Claudio Pellini [a], Nicolò Pianta [a,*], Daniele Callegari [b,c], Gualtiero Conte [a], Roberto Lorenzi [a], Cataldo Simari [c,d], Martina De Bonis [d], Silvia Leonardi [e], Zenonas Jusys [f,g], Julio César Espinosa-Angeles [f,g], Dominic Bresser [f,g,h], Piercarlo Mustarelli [a,c], Riccardo Ruffo [a,c]

[a] Department of Materials Science, University of Milano - Bicocca, Via R. Cozzi 55, Milan I-20125, Italy
[b] Department of Chemistry, University of Pavia, Via Taramelli 16, Pavia 27100, Italy
[c] GISEL - Centro di Riferimento Nazionale per i Sistemi di Accumulo Elettrochimico di Energia, Florence, 50121, Italy
[d] Department of Chemistry, University of Calabria, Arcavacata di Rende (CS), 87036, Italy
[e] Eni DE-R&D, Via Fauser 4, 28100 Novara, Italy
[f] Helmholtz Institute Ulm (HIU), Helmholtzstrasse 11, Ulm, 89081, Germany
[g] Karlsruhe Institute of Technology (KIT), 76021 Karlsruhe, Germany
[h] Ulm University (UUlm), 89069 Ulm, Germany

ARTICLE INFO

Keywords:
Aqueous lithium-ion electrolytes
Dimethyl sulfoxide (DMSO)
Highly concentrated electrolytes
Low-temperature battery performance
Solvation structure and ion transport

ABSTRACT

Aqueous electrolytes for lithium-ion batteries offer a safer and more environmentally friendly alternative to flammable organic electrolytes. One of the main challenges, however, is their narrow electrochemical stability window, which is typically widened by using highly concentrated salts, sometimes combined with organic solvents. Dimethyl sulfoxide (DMSO) stands out among organic solvents used in this context due to its affordability, low toxicity, and safe handling. Additionally, DMSO and water form solutions that remain in the liquid state at extremely low temperatures (down to -130 °C). In this study, we designed and characterized three electrolytes by mixing water and DMSO and incorporating lithium bis(fluorosulfonyl)imide (LiFSI) at three different concentrations. The resulting electrolytes exhibited exceptional thermal and electrochemical stability. Furthermore, we provided a detailed analysis of their solvation structure, intermolecular interactions and transport properties. Finally, we evaluated these electrolytes in a full-cell configuration with $LiTi_2(PO_4)_3$ and $LiMn_2O_4$, testing their performance at room temperature (100 cycles, 1.5 V, 40 Wh kg_{AM}^{-1}, where AM stands for active mass, and refers to the sum of the active masses of both anode and cathode active materials) and at -10 °C (50 cycles, 1.3 V, 15 Wh kg_{AM}^{-1}).

1. Introduction

Lithium-ion batteries (LIBs) are one of the most widespread energy storage devices employed in various applications [1–3]. However, to maintain high energy performance, they typically utilize flammable and toxic electrolyte components, which can pose safety [4] and disposal [5] concerns. Typically, LIBs consist of a lithiated carbonaceous negative electrode and a transition metal oxide positive electrode, separated by a flammable organic electrolyte. The high flammability of the electrolyte, combined with the possibility of releasing oxygen at high temperatures from the cathode, makes the typical LIB prone to events such as fires or explosions, especially following overcharging or crash [4,6].

A promising alternative is the use of water-based electrolytes, which are inherently safer, more environmentally friendly, and less expensive than non-aqueous alternatives. However, the narrow electrochemical stability window (ESW) of water (only 1.23 V) limits electrode selection and restricts the energy density of aqueous LIBs. Several strategies have been proposed to address this issue, one of the most effective being the addition of salt until a superconcentrated regime is reached. When the salt concentration exceeds the amount of water, the system is referred to as a "Water-in-Salt" Electrolyte (WISE) [7]. In such solutions, the number of ions is so high that water molecules are insufficient to fully solvate them. As a result, if all water molecules are locked in an ion's solvation shell, their decomposition reactions become more difficult, leading to an increase in overpotential and a subsequent expansion of the ESW [8–10].

Therefore, selecting appropriate salt is a crucial step in designing an aqueous electrolyte. The salt must be highly soluble in water to enable

* Corresponding author at: via R. Cozzi 55 20125 Milan Italy.
E-mail address: nicolo.pianta@unimib.it (N. Pianta).

https://doi.org/10.1016/j.electacta.2025.146903
Received 14 April 2025; Received in revised form 30 June 2025; Accepted 11 July 2025
Available online 12 July 2025

superconcentration and should also promote the formation of the solid electrolyte interphase (SEI) layer. The SEI is a passivation layer formed by the reduction of the electrolyte on the electrode surface. It protects the electrolyte from further degradation while allowing Li^+ ions to move between the electrodes. In aqueous electrolytes, the SEI layer is primarily composed of LiF, which originates from the reduction of lithium fluorinated salts such as lithium bis(fluorosulfonyl)imide (LiFSI), lithium bis(trifluoromethanesulfonyl)imide (LiTFSI), and lithium triflate (LiOTF) [11,12]. In general, LiFSI is able to produce a compact and mostly inorganic SEI, especially at high concentration [13,14]. Furthermore, it has been proven to be beneficial in the formation of a stable SEI in aqueous electrolytes [15]. By combining superconcentration with SEI-forming agents, it is possible to extend the ESW of water-based electrolytes up to 3 V or even higher [7,16,17].

Another approach to enhance SEI-layer formation and expanding the ESW is the addition of a co-solvent to the electrolyte formulation. The reduction of certain organic solvents in the presence of Li^+ ions can generate key SEI compounds such as Li_2CO_3 and various lithium alkylcarbonates [18]. Moreover, in pure aqueous electrolytes, a thin layer of water molecules adsorbs onto the electrode surface (Inner Helmholtz Plane, IHP), where electron transfer and redox decomposition reactions occur easily [19]. When a co-solvent is introduced, some of the water molecules in the solvation shells and at the IHP are replaced by the co-solvent, thereby hindering water decomposition. Additionally, the use of a co-solvent can reduce the amount of salt required to lock water molecules and improve the electrochemical stability of water, lowering the overall electrolyte cost.

Suitable co-solvents should be electrochemically stable and miscible with water. Some of the most promising studies in literature have explored hybrid aqueous/non-aqueous strategies, pairing water with acetonitrile [20], sulfolane [21], carbonates [22], glycols [23,24], or even combinations of these [25], achieving ESWs greater than 4 V. However, many of these solvents are flammable, hazardous to use, or highly toxic, which compromises the primary safety benefits of water-based electrolytes.

In contrast, dimethyl sulfoxide (DMSO) is almost non-toxic, hardly flammable, inexpensive, and safe to handle [26], as demonstrated by its NFPA 704 ratings, reported in figure S1. It also exhibits good thermal stability [27] and, due to its high polarity, can dissolve a wide range of salts, making it useful in various applications [28]. Additionally, it is fully miscible with water in any ratio and can form a eutectic solution that remains liquid even at extremely low temperatures [29].

Here, we present a study on the physicochemical and electrochemical properties of three electrolytes composed of water, DMSO, and LiFSI in different molar ratios, with a focus on how intermolecular interactions influence these properties. In addition, we evaluated these electrolytes in a $LiTi_2(PO_4)_3$ | electrolyte | $LiMn_2O_4$ full-cell configuration at both room temperature and −10 °C, taking advantage of the low freezing point of the water/DMSO mixture.

2. Experimental

2.1. Sample preparation

The reagents used for the preparation of the electrolytes were: Milli-Q water ($\sigma = 6.7$ μS cm^{-1}), dimethyl sulfoxide (DMSO, >99 %, Fluorochem), and lithium bis(fluorosulfonyl)imide (LiFSI, 99.9 %, Solvionic). Water and DMSO were weighed and mixed in a fixed 1:1 molar ratio, while the amount of LiFSI varied for each electrolyte, resulting in three different samples with molar ratios of 1:1:x, where $x = 0.5$, 1, or 1.5. The salts were then fully dissolved by sonication and the electrolytes were stored at room temperature.

To simplify sample coding, the ratios were expressed as whole numbers, and each component was denoted by a single letter (D for DMSO, w for water, and F for LiFSI). Accordingly, the three resulting sample names were: DwF221, DwF222, and DwF223.

Carbon-coated $LiTi_2(PO_4)_3$ (LTP) was synthesized using a straightforward one-pot synthesis method. First, $NH_4H_2(PO_4)_3$ was dissolved in ethanol under stirring, followed by the dropwise addition of $Ti(OC_4H_9)_4$, ensuring complete dissolution before each addition. $CH_3COOLi \times 2H_2O$ and $C_6H_{12}O_6$ were added as lithium and carbon sources, respectively. The mixture was stirred for 4 h at 55 °C in a sealed container, then opened and heated to 80 °C to evaporate ethanol and form a gel. After a final drying step at 100 °C, the precursor was ground in a mortar to obtain a fine powder, which was subsequently heated at 800 °C for 6 h under an argon atmosphere.

In contrast, a commercial $LiMn_2O_4$ (LMO) powder (Sigma-Aldrich) was used.

The electrodes for electrochemical studies were prepared from slurries consisting of active materials (LMO/LTP), carbon black (SuperP, Erachem Comilog, Inc.), and polyvinylidene fluoride (PVDF 6020, Solvay) as a binder, mixed in N-methyl-2-pyrrolidone. For LTP, the weight ratio of these components was 7:2:1, and the slurry was cast onto an aluminum foil, while for LMO, the ratio was 8:1:1, applied to a carbon-coated aluminum (CC-Al) foil. The resulting final mass loadings were 2.1 mg cm^{-2} for LTP and 2.8 mg cm^{-2} for LMO.

2.2. Electrochemical characterization

The ionic conductivity of the electrolytes was measured using potentiostatic electrochemical impedance spectroscopy (PEIS) with a dip probe cell containing two platinum foils in a glass casing, featuring a cell constant of 1.04 cm^{-1}. Measurements were performed over a frequency range of 100 Hz to 300 kHz with a signal amplitude of 10 mV. PEIS spectra were recorded at various temperatures, from −35 °C to 80 °C in 5 °C increments, using a climatic chamber (Angelantoni, Italy). Conductivity was calculated from the second Ohm's law, using the real part of the impedance at high frequency as resistance (see Figure S3).

The ESW measurements were conducted using a three-electrode Swagelok cell, with a silver/silver chloride (AgCl/Ag, 3.5 M KCl) reference electrode (RE) and a free-standing activated carbon (F400, for more information see [30]) disc as the counter electrode (CE). Three different working electrodes (WEs) were tested and compared: aluminum, carbon-coated aluminum, and stainless steel. The ESW was determined through two Linear Sweep Voltammetry (LSV) steps: the first toward negative potential to assess cathodic stability, followed by a spontaneous return to the starting potential, and the second toward positive potential to evaluate anodic stability. Both steps were conducted at room temperature with a scan rate of 0.5 mV s^{-1}. These results also helped determine the most suitable current collectors (CC) for the two extremes of the ESW of the electrolytes.

The electrochemical behavior of the LTP and LMO electrodes was examined through Cyclic Voltammetry (CV) measurements at a scan rate of 0.1 mV s^{-1}, using a setup similar to that of the LSVs. The three-electrode Swagelok cell featured AgCl/Ag as the RE and activated carbon as the CE. The WE configuration depended on the active material under investigation: LTP was tested on an Al disc and Al rod, while LMO was evaluated on a CC-Al disc and a glassy carbon rod.

Constant-current cycling tests were performed in R2032 coin cells, using LTP on Al as the negative electrode and LMO on CC-Al as the positive electrode, with a slight excess in the active mass of the positive electrode (1.34:1 with respect to that of LTP) so to account for any irreversible reaction that occurs in the first cycles. A Whatman glass microfiber separator filled with approximately 100 μL of electrolyte was used. Additionally, an Al foil was placed between the negative electrode and the stainless-steel spacer, while a CC-Al foil was positioned between the positive electrode and the stainless-steel cap.

Impedance spectra have been performed on a partially charged cell (state of charge: 20 %) three electrode cells composed by LMO and LTP operative electrodes and AgCl/Ag reference electrode at 30 and −10 °C.

2.3. Physicochemical characterization

The thermal properties of the electrolytes were analyzed using Differential Scanning Calorimetry (DSC) over a temperature range of −120 °C to 80 °C. A Mettler Toledo DSC 1 Star® instrument, cooled with liquid nitrogen and controlled via STARe® software, was used. The analysis followed a four-step protocol: (1) an isothermal step at 30 °C for 10 min to equilibrate the system, (2) a cooling phase from 30 °C to −120 °C at a rate of −5 °C min^{-1}, (3) a 10-minute isothermal step at −120 °C, and (4) a heating phase from −120 °C to 80 °C at a rate of +5 °C min^{-1}.

Viscosity measurements were performed using an Anton Paar Rheometer MCR 92 with a parallel plate geometry (25 mm diameter). For each electrolyte, viscosity was measured at a constant shear rate of 10 s^{-1} while varying the temperature from 5 °C to 80 °C in 5 °C increments, with each step lasting 4 min.

Raman spectroscopy was conducted using a Labram Dilor spectrometer (Jobin Yvon) in a backscattering configuration with a 488 nm Ar^{+} laser and a resolution of 2 cm^{-1}. The laser beam was focused on a circular spot using a long-working-distance microscope objective with 50 × magnification and a numerical aperture of 0.60. All spectra were collected at room temperature through three accumulations of 30 s of integration time.

The thermal stability of the full cell was assessed using Accelerated Rate Calorimetry (ARC-ES, Thermal Hazard Technology). Prior to ARC testing, the coin cells were charged to a maximum potential of 2.1 V at a rate of 0.5 C. The accelerated rate calorimeter operated in heat-wait-search (HWS) mode with a sensitivity threshold of 0.02 °C min^{-1}. Tests were performed over a temperature range of 30–280 °C, with stepwise increments of 5 °C and an equilibration time of 15 min per step.

A Bruker AVANCE 300NMR Wide Bore spectrometer equipped with a Diff30 Z-diffusion 30 G/cm/A multinuclear probe with substitutable RF inserts has been employed for NMR measurements. Spin-lattice relaxation times (T_1) were determined using the inversion recovery sequence (π-τ-π/2). On the other hand, self-diffusion coefficients were measured using the pulsed field gradient stimulated echo (PFG-STE) method [31]. The sequence is composed by three 90° RF pulses (π/2-τ1-π/2-τm-π/2) and two gradient pulses that are applied after the first and the third Rf pulses and the resulting echo has been acquired at time τ=2τ1+τm. The magnetic field pulses have their magnitude (g), duration (δ) and time delay (Δ) reported in the Stejskal–Tanner expression, which has been employed to analyze the Fourier-transformed echo decays:

$$I = I_o\ e^{-\beta D} \tag{1}$$

Where I and I_0 indicate the intensity or area of selected resonance peaks, respectively, in the presence and absence of gradients. β is the field gradient parameter defined as $\beta=[(\gamma g\delta)^2 \times (\Delta-\delta/3)]$ and D is the measured self-diffusion coefficient. The experimental parameters for the investigated samples were: δ=0.8–3 ms, Δ=8–30 ms and the gradient amplitude has been varied from 200 to 900 Gauss cm^{-1}. The uncertainties in the self-diffusion measurements are approximately 3 %. Measurements were carried out in the temperature range 20–60 °C, with increments of 10 °C and leaving each sample to equilibrate for 10 min at each temperature achieved. To avoid contact with moisture, samples were prepared in a glow box under inert atmosphere and hermetically sealed in 5 mm Pyrex tubes.

For Differential Electrochemical Mass Spectrometry (DEMS) measurements, a leakless AgCl/Ag was used as reference electrode and AC coated on both sides of Al foil was utilized as counter electrode. The DEMS set-up was described in detail in refs [32,33], equipped with a quadrupole mass spectrometer (Pfeiffer Vacuum, QMS 410) and the potential control was achieved by an electrochemical workstation (Princeton Applied Research (PAR) 263A). Measurements have been performed using either titanium film (ca. 100 nm) sputtered onto a 50 μm thick fluoroethylene-propylene (FEP) membrane (Bohlender, Bola) of that coated with a slurry of Super C65 carbon with 10 wt.% PVDF as the working electrodes, with back side of the membrane exposed directly to the ultrahigh vacuum system of the mass spectrometer. Two electrolyte solutions have been analyzed: both the hybrid solution labelled DwF223 and a 1 M Na_2SO_4 aqueous solution, which was used as benchmark.

3. Results and discussion

Several characterizations of water/DMSO hybrid electrolytes were performed to assess their physicochemical properties, correlate them with their solvation structure, and ultimately evaluate their suitability for lithium-ion battery applications.

The thermal properties of the three electrolytes were analyzed using Differential Scanning Calorimetry (DSC, Fig. 1a and S2 for heating and cooling, respectively). All electrolytes exhibited a glass transition between −100 °C and −80 °C, characteristic of highly viscous liquids. The glass transition temperature (T_g), reported in Table 1, depends on electrolyte concentration: as the concentration increases, T_g also rises. In the most concentrated electrolyte (DwF223), stronger molecular interactions lead to higher cohesion, requiring more energy for the transition from the glassy to the liquid state [34].

Notably, aside from the glass transition, no other thermal events were observed within the investigated temperature range, particularly no crystallization. This indicates that neither water nor DMSO solidified at the extremely low temperatures to which they were exposed, due to the strong molecular interactions within this system. As further elaborated in the Raman analysis, water and DMSO molecules establish strong interactions, maintaining the liquid state even at low temperatures [29]. Additionally, the strong bonds between the solvent molecules and ions hinder the solidification, a well-known phenomenon known as freezing-point depression.

The ionic conductivity of the three electrolytes was measured as a function of temperature (Fig. 1b, example impedance spectrum in Fig. S3). An increase in salt concentration resulted in a decrease in ionic conductivity, which dropped from 8.9 to 1.2 mS cm^{-1} at room temperature (Table 1). In general, for strong electrolytes, conductivity (σ) increases with salt concentration due to a higher number of charge carriers in solution. However, beyond a certain threshold—where the electrolyte enters the super-concentration regime—further salt addition leads to a decrease in conductivity.

The conductivity (σ) of an electrolyte is governed by the physical characteristics of its charge carriers, as expressed by the Eq. (2) [35]:

$$\sigma = \sum_i F z_i c_i \mu_i \tag{2}$$

where F is the Faraday constant, i represents a specific charge carrier (ion, hole, or electron), c_i is its concentration, z_i is its charge, and μ_i is its electrical mobility. The reduction in ionic mobility at high concentrations follows the principle underlying Kohlrausch's law and becomes particularly significant in concentrated systems. This decrease in mobility arises primarily from two factors [36]: (i) Increased viscosity: solvent molecules arrange into solvation shells around ions, creating larger species in solution. This effect is particularly pronounced in highly concentrated solutions, where a substantial number of these structures are present; (ii) Formation of Contact-Ion Pairs (CIPs): in superconcentrated solutions, the available solvent molecules are insufficient to fully solvate all ions, leading to the formation of large clusters composed of one cation, one anion, and solvent molecules. These clusters, which carry a net charge of zero, hinder charge transport.

The complex interactions between solvent molecules and ions are also behind the temperature-dependent conductivity trend, which deviates from the normal Arrhenius-like trend and instead follows a Vogel-Tammann-Fulcher (VTF)-like trend, in particular at low temperature, because the more the temperature approaches the T_g, the more that deviation is pronounced [37]. The VTF equation (Eq. (3)) was used to fit

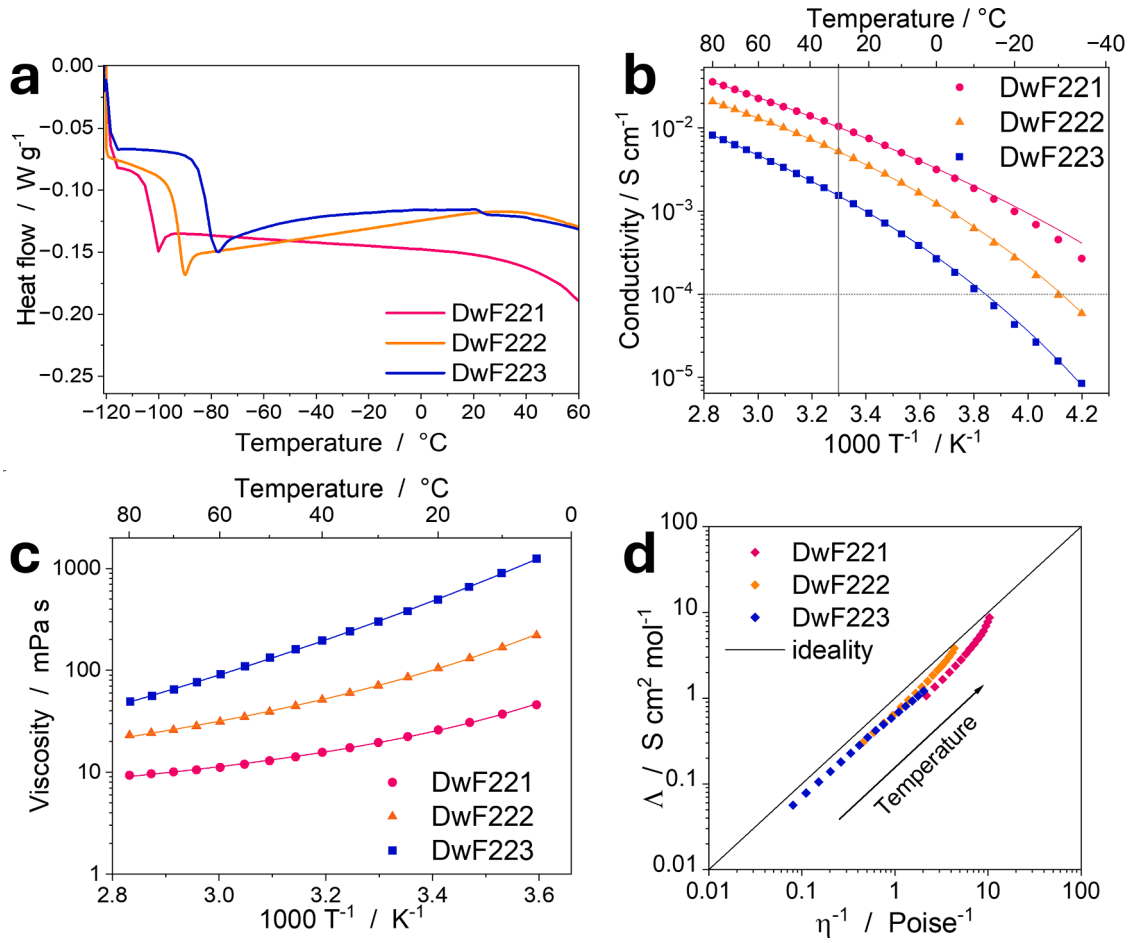

Fig. 1. Physicochemical characterizations of the electrolytes: (a) Differential Scanning Calorimetry (DSC); (b) temperature dependance of ionic conductivity (scattered points) and VTF fittings (solid lines); (c) temperature dependence of viscosity (scattered points) and VTF fittings (solid lines); (d) Walden plot.

Table 1
Summary of some of the main physicochemical properties of the electrolyte under study. The table features the pseudo-activation energies calculated for conductivity ($E_{pa,\sigma}$) and viscosity ($E_{pa,\eta}$), glass transition (T_g) and T_0 for conductivity, value of the conductivity at room temperature and concentration, expressed in molality.

Electrolyte	$E_{pa,\sigma}$ / eV	$E_{pa,\eta}$ / eV	T_g / °C	T_0 / °C	σ at 25 °C / mS cm^{-1}	[LiFSI] / mol kg^{-1}
DwF221	0.063	0.015	−106	−121	8.92	5.2
DwF222	0.066	0.030	−97	−112	4.33	10.4
DwF223	0.085	0.110	−87	−116	1.22	15.6

the conductivity data, with best-fitted curves shown in Fig. 1b:

$$\sigma = \sigma_o \exp\left(\frac{-E_{pa,\sigma}}{k_B(T - T_0)}\right) \quad (3)$$

where T is the experimental temperature, T_0 is a parameter related to the glass transition temperature (often referred to as the vanishing mobility temperature or theoretical glass transition temperature), σ is the measured conductivity, σ_0 is a pre-exponential factor associated with the number of charge carriers [38] and $E_{pa,\sigma}$ is a pseudo-activation energy related to charge transport, similar to the Arrhenius activation energy [39]. The main VTF fitting parameters (i.e. $E_{pa,\sigma}$ and T_0) are listed in Table 1.

While $E_{pa,\sigma}$, T_g, and conductivity trends align with the expected reduction in ion mobility as salt concentration increases, T_0, which represents the temperature at which charge carriers cease movement [40], does not always follow the same pattern, remaining relatively independent of salt content. Conversely, T_g is linked to the overall flow of species in solution and decreases as salt concentration rises. The divergence in these trends suggests a partial decoupling between charge transport and bulk solution friction [41,42].

The viscosity of the electrolytes was also measured as a function of temperature (Fig. 1c). As the concentration of LiFSI increases, the number of large solvation clusters also increases, thereby hindering ion mobility and raising viscosity.

Moreover, the DSC-derived T_g values align with the viscosity trends. The electrolyte with the best transport properties — i.e., highest conductivity and lowest viscosity — is the DwF221, which also exhibits the lowest T_g. This suggests that higher mobility within the solution correlates with lower energy requirements for the glass-to-liquid transition.

Temperature-dependent viscosity also follows a VTF behavior (Eq. (4)), analogous to conductivity:

$$\eta = \eta_o \exp\left(\frac{E_{pa,\eta}}{k_B(T - T_{0,\eta})}\right) \quad (4)$$

where η_0, $E_{pa,\eta}$, and $T_{0,\eta}$ are fitting parameters similar to those in the VTF conductivity model. The difference between $E_{pa,\sigma}$ and $E_{pa,\eta}$ (Table 1) suggest a decoupling of conductivity and viscosity mechanisms. Viscosity appears to be more strongly influenced by salt concentration than conductivity, possibly due to neutral clusters (CIPs) containing both Li^+ and FSI^-, or other solvent-salt structures that facilitate ion movement in highly concentrated solutions [41].

Viscosity and conductivity are related by the Walden rule, which states that their product remains constant. The Walden plot (Fig. 1d)

graphically represents this relationship and helps assess ion interactions within the electrolytes. The solid black line represents an ideal, fully dissociated electrolyte (e.g., 0.01 M KCl in water). The aqueous/DMSO electrolytes in this study demonstrate good ionic character, approaching ideality as temperature increases [43].

Conductivity measurements reveal a general deceleration of ionic transport with increasing salt concentration but lack the capacity to discern species-specific dynamics. To elucidate the interrelationships among the Li-ion conduction, Li^+ solvation structure, and solution viscosity, PFG-NMR were employed to determine the self-diffusion coefficients of individual solution components. Specifically, the diffusivities of ^1H, ^7Li, and ^{19}F were measured separately as a function of salt concentration (Fig. 2a), which correspond to the motion of solvent molecules (H_2O and DMSO), lithium cations (Li^+), and bis(fluorosulfonyl)imide anions (FSI^-), respectively. As anticipated, increasing solution viscosity results in a reduction in the self-diffusion coefficients of all components.

Notably, H_2O molecules are the most mobile species across the entire concentration range, with their diffusivity significantly exceeding that of DMSO and the ions. This contrasts with previous literature demonstrating significant water coordination to Li^+ ions [44–46]. To solve this apparent paradox, we can hypothesize that the water-Li^+ binding is highly dynamic and short-lived. Under these conditions, the rapid exchange of water between Li^+ coordination sites, rather than the presence of free water, accounts for the observed differential diffusion rates. On the other side, the similar diffusivities of Li^+, DMSO and FSI^- imply longer residence times for the two ligands with lithium. Above 5.2 m concentration, a surprising phenomenon was observed with Li^+ diffusing faster than DMSO. The temperature evolution for self-diffusion coefficients of solvents and ions in the three systems further confirms this trend (see Supplementary Fig. S4). To clarify this phenomenon, Fig. 2b presents the ratios of self-diffusion coefficients (D_{water}/D_{Li}, D_{DMSO}/D_{Li}, and D_{FSI}/D_{Li}) as a function of concentration. Both D_{DMSO}/D_{Li} and D_{FSI}/D_{Li} approach unity and decrease with increasing concentrations. The observed acceleration of Li^+ diffusion relative to DMSO and FSI^- in concentrated electrolytes strongly indicates rapid Li^+ exchange between the coordination sites formed by the two ligands (DMSO and FSI^-), providing direct evidence for a concentration-dependent shift towards a Li^+ hopping mechanism within the DMSO:H_2O:LiFSI system. This observation is consistent with previously reported hopping conduction in sulfolane-based highly concentrated electrolytes [47,48]. The decrease in the ratio between D_{FSI} and D_{Li} generally implies an increasing lithium transference number (t_{Li+}) with LiFSI concentration, as also described in detail below.

Although it is known that the Nernst-Einstein equation becomes less reliable as the ion-ion interactions increase in strength (i.e., at very high concentrations), we still decided to use it to extract an estimate of parameters such as transport number etc., in order to get a clearer idea of the electrolyte and its properties. It is also important to note that not all concentrated electrolytes deviate totally from ideality, as we could see in a previous work, where a 20 mol kg^{-1} solution of potassium acetate in water was shown to follow Kohlrausch's law [49], strengthening us in

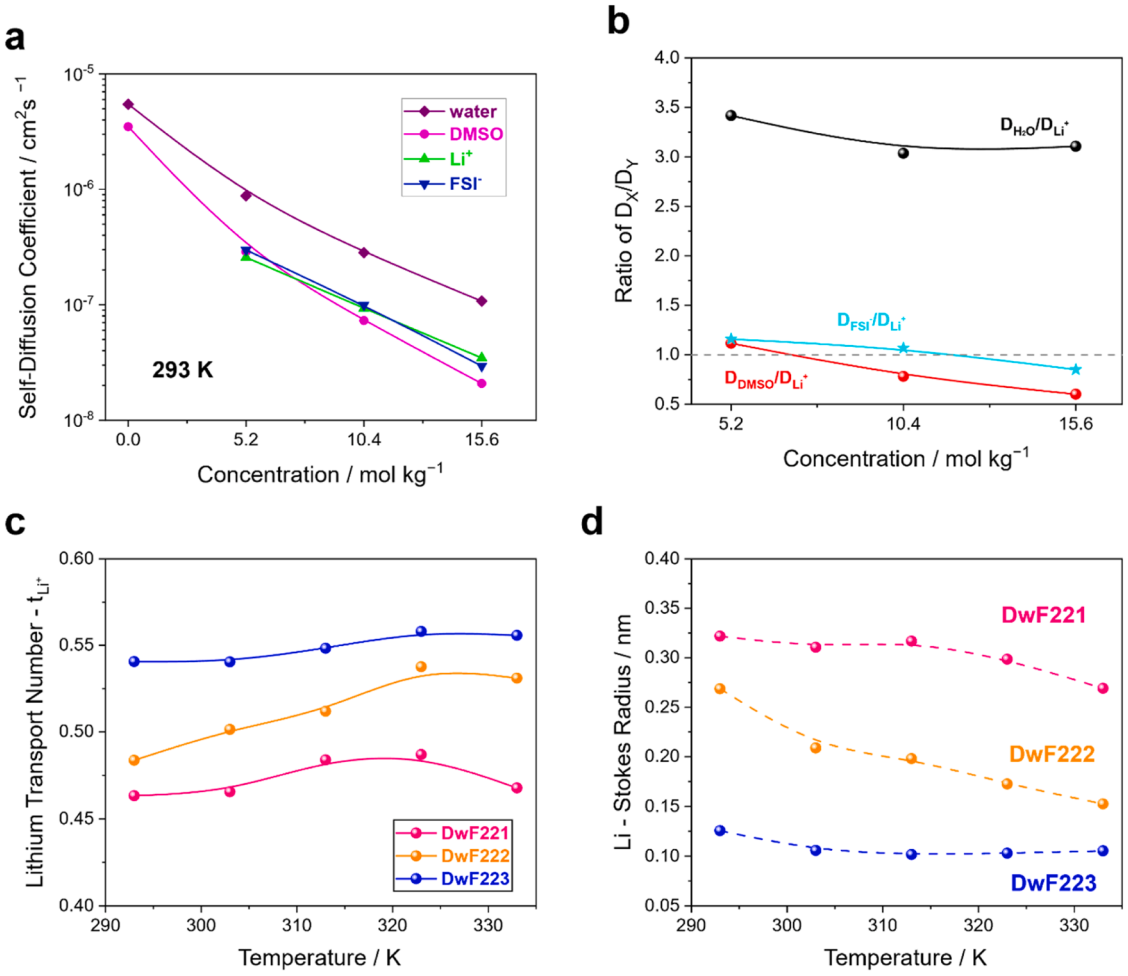

Fig. 2. (a) Concentration dependence of self-diffusion coefficients for the solvents, lithium and FSI ions of LiFSI in H_2O:DMSO. (b) Concentration dependent diffusivity ratios (R) of Li^+ in DMSO:H_2O:LiFSI. Filled squares D_{H2O}/D_{Li+}, filled circles D_{DMSO}/D_{Li+}, filled stars D_{FSI-}/D_{Li+}. (c) Lithium-ion transference number and (d) Stokes radii for the electrolytes determined by the NMR method.

the idea that the approximation may be at least partially valid.

The apparent lithium transference number (t_{Li+}), which provides a valuable estimate of the lithium ion's contribution to charge transport, was calculated from the experimental self-diffusion coefficients of Li^+ and FSI^- ions according to Eq. (5) and reported in Fig. 2c and Table 2.

$$\tau_{Li+} = \frac{D_{Li+}}{D_{Li+} + D_{FSI-}} \quad (5)$$

The apparent t_{Li+} for all the three electrolytes range between 0.45 and 0.55, typical values for superconcentrated electrolyte solutions [47, 50] and higher than those observed in conventional organic aprotic solutions [51–56]. It can be seen that the t_{Li+} increases with salt concentration due to major contribution and/or higher efficiency of the aforementioned Li^+ hopping mechanism. Notably, the values are practically temperature independent for the DwF221 and DwF223 electrolytes suggesting their predominant transport mechanism (vehicular for DwF221 and hopping for DwF223), is thermally stable and not significantly altered by changes in thermal energy within this temperature range. Contrariwise, the clear temperature dependence for DwF222 indicates a shift from a solvent-assisted vehicular mechanism to a hopping mechanism facilitated by thermal activation. By combining viscosity and diffusion coefficient data, the Stokes-Einstein equation yielded effective hydrodynamic radii for Li^+ ranging from 0.32 for DwF221 to 0.13 nm as in the case of DwF223 (Fig. 2d). The DwF223 values approach the Van der Walls radius of Li^+ ion (i.e., 0.073 - 0.090 nm) suggesting a weak solvation shell and rapid ligand exchange, further supporting the prevalence of a Li^+ hopping mechanism.

The degree in cation–anion dissociation can be assessed by comparing ionic conductivity from impedance spectroscopy (σ_{EIS}) and that calculated from self-diffusion coefficients (σ_{NMR}) using the Nernst–Einstein formula (*Eq. (6)*):

$$\boldsymbol{\sigma_{NMR}} = \left(\frac{\boldsymbol{F^2 c_{salt}}}{\boldsymbol{R \cdot T}}\right)(\boldsymbol{D_{Li}} + \boldsymbol{D_{FSI}}) \quad (6)$$

where D_{Li} and D_{FSI} are the lithium and fluorine diffusivity, respectively, F is the Faraday constant and "*c*" is the molar concentration of electrolytes.

The $\sigma_{EIS}/\sigma_{NMR}$ ratio quantifies the contribution of charged ions to ionic conduction from all the diffusing species, on the time scale of the measurement. Notably, σ_{NMR} typically exceeds the experimental σ_{EIS}, since not all of the diffusive species, such as neutral ion clusters, contribute to the charge transport, as in the case of Contact-Ion-Pairs. Ionicity index (Table 2) decreases with increasing salt concentration. This trend, from 0.63 for DwF221 to 0.23 for DwF223, has to be ascribed to stronger Coulombic interaction between cations and anions at higher salt concentrations [57].

Spin-lattice relaxation times (T_1) analysis provided additional insights into molecular-scale interactions between solvent molecules (^1H) and ions (^7Li for Li^+ and ^{19}F for FSI^-). Indeed, T_1 is indicative of molecular roto-translational mobility, reflecting the impact of molecular movements on the energy transfer between nuclear spins and the lattice. In essence, the stronger the interactions the lower the molecular mobility (thus, shorter T_1). Compared to pure solvents, the lower T_1 values for H_2O and DMSO in mixture (Supplementary Fig. S5) suggest stronger electrostatic interactions, potentially involving "improper hydrogen bond" formation between water and DMSO methyl groups, which will be further examined via Raman spectroscopy. The temperature dependence of Li^+ and FSI^- values (Fig. 3a, b), reveals the highest mobility DwF221 (longest T_1). Converging diffusivity data, ionicity index, with this evidence, we may infer that Solvent-Separated Ion Pairs (SSIPs) largely dictate the ion-solvent structure of the electrolyte. At higher LiFSI concentrations there is a clear drop in the T_1 values indicating restricted ions motions. This is likely due to the contact and/or aggregating ion pairs formation characterized by strong electrostatic interaction between Li^+ ion and FSI^-.

The Raman analysis provides insights into the arrangement of molecules in solution, leading to the formation of distinctive solvation structures. The complete spectra are presented in Fig. S6, while below these will be shown and discussed in three separate regions of particular importance for the DMSO/water system. The range between 600 and 800 cm^{-1} (Fig. 4a) provides valuable information mostly regarding the behavior of the ions. The region around 1000 cm^{-1} is useful in understanding the interactions between the two solvents (Fig. 4b), while the third region, around 3000 cm^{-1} (Fig. 4c), helps the comprehension of both solvent and salt interactions.

Pure DMSO presents two peaks in the 700 cm^{-1} region: at 668 cm^{-1} and 698 cm^{-1} that correspond to symmetric and asymmetric C-S-C stretching, respectively [58]. When DMSO is mixed with water in a 1:1 molar ratio, both these peaks shift 5 and 9 cm^{-1} toward higher wavenumbers, respectively. This indicates that the coordination of DMSO with its chemical environment is significantly different because it interacts with water molecules. In particular, the frequency shifts are primarily caused by the formation of hydrogen bonds between the oxygen atom of DMSO and a hydrogen atom of water, rather than by self-association of DMSO molecules. The formation of these hydrogen bonds reduces the electronegativity of the DMSO oxygen atom and increases the sulfur electronegativity, thus strengthening the CSC bonds. As a result, bond shortening is associated with an increase in the force constant, which in turn leads to a blue shift in vibrational frequencies, as observed for the CSC stretching frequencies [59]. The same peaks undergo similar changes after addition of LiFSI salt (upper three plots in Fig. 4a), indicating that DMSO intermolecular interactions are also affected by the presence of LiFSI. Moreover, in the spectra with the salt a third peak appears, between 730 and 750 cm^{-1}, which is attributed to the S-N-S scissoring vibration of LiFSI [60]. This peak undergoes a significant blueshift, depending on the salt concentration. As the salt concentration increases, the number of available solvent molecules in the solution decreases, passing from the Solvent Separated Ion Pairs (SSIP) solvation structure to the formation of new ones, as Contact Ion Pairs (CIP), where one cation and one anion share a shell, and aggregates (AGG), where multiple ions form a single shell [61]. There is clear transition from SSIP to CIP/AGG structures, as evidenced by the significant shift of the LiFSI peak. The peak moves from 732 cm^{-1} in the most diluted electrolyte to 749 cm^{-1} in the most concentrated one, in agreement with the peak position registered for SSIP and AGG species, respectively [62].

Table 2
Conductivity measured though impedance spectroscopy and PFG NMR, degree of dissociation (Ionicity), and lithium transference number for all three electrolyte systems as a function of temperature.

T / °C	DwF221				DwF222				DwF223			
	σ_{NMR} / mS cm^{-1}	σ_{EIS} / mS cm^{-1}	Ionicity	t_{Li+}	σ_{NMR} / mS cm^{-1}	σ_{EIS} / mS cm^{-1}	Ionicity	t_{Li+}	σ_{NMR} / mS cm^{-1}	σ_{EIS} / mS cm^{-1}	Ionicity	t_{Li+}
20	11.92	7.49	0.63	0.46	8.25	3.47	0.42	0.48	4.12	0.95	0.23	0.54
30	19.76	10.5	0.53	0.47	14.61	5.22	0.36	0.50	8.08	1.55	0.19	0.54
40	28.83	14.05	0.49	0.48	20.27	7.4	0.37	0.51	12.60	2.37	0.19	0.55
50	39.49	18.11	0.46	0.49	28.38	10.11	0.36	0.54	18.11	3.35	0.19	0.56
60	55.39	22.8	0.41	0.47	40.00	13.13	0.33	0.53	25.89	4.68	0.18	0.56

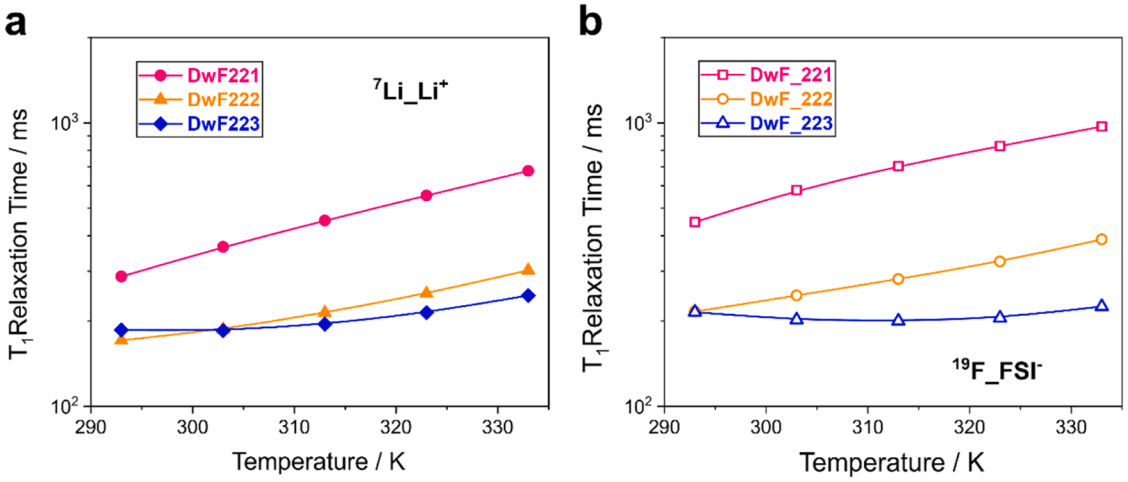

Fig. 3. The temperature evolution of T_1 relaxation for (a) Li+ and (b) FSI- in the DMSO:H2O:LiFSI electrolytes.

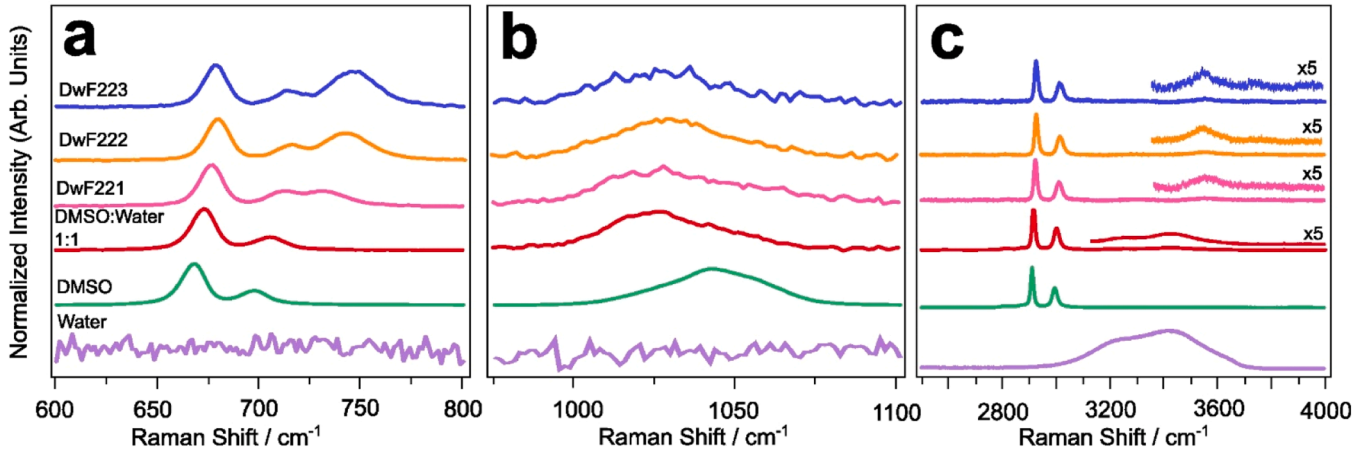

Fig. 4. Raman spectra of the systems under analysis, separated in three regions: (a) from 600 to 800 cm^{-1}, (b) from around 1000 to 1100 cm^{-1} and (c) from around 2600 to 4000 cm^{-1}.

Fig. 4b shows the peak around 1040 cm^{-1}, relative to the *S=O* stretching of DMSO. In pure DMSO, this peak is the combination of four sub-bands [63]: DMSO molecules that form a linear dimer (around 1025 cm^{-1}), DMSO molecules that form cyclic dimer (in-phase and out-phase, around 1040 and 1058 cm^{-1}, respectively), and monomeric DMSO molecules (near 1070 cm^{-1}). With the addition of water, a new peak in the *S=O* stretching band appears at about 1015 cm^{-1}, related to the H bonds [64]. A comparison of the deconvolutions of this peak in pure DMSO and in the 1:1 solution with water, Fig. S7 of the Supporting Information, reveals that the addition of water causes a red-shift from 1043 to 1024 cm^{-1} in the *S=O* stretching band. Differently from the C-S-C bonds, *S=O* is weakened by the formation of H-bonds, causing a big red shift instead of a blue one.

In the 3000 cm^{-1} range there are the O-H stretching broad band, which is located between 3000 and 3700 cm^{-1} for water, and the C-H stretching peaks, which are situated near 2900 and 3000 cm^{-1} for DMSO, which are of particular interest. Water molecules can form a wide range of hydrogen bonds, namely from zero to four, due to their high degree of intermolecular interaction. The OH band of water is characterized by a broad spectrum due to the presence of multiple sub-bands, which are attributed to these various types of interactions [65,66].

The main and most prominent peaks in water spectrum, at 3242 and 3441 cm^{-1}, correspond to the stretching of the O-H bond of water molecules, which can form four or three hydrogen bonds, respectively [65]. In the water:DMSO=1:1 solution, O-H signals are very low compared to C-H signals merely because of the lower concentration, but it is still possible to recognize the presence of the same bands visible in pure water. This indicates that water molecules form almost the same number and type of hydrogen bonds even when half of the water molecules are replaced by DMSO, suggesting that water is also able to form hydrogen bonds with DMSO, as also stated before. It has been previously reported that DMSO and water form two distinct aggregates, namely 1DMSO-2-water and 2DMSO-1water, with a predominance of the latter in a 1:1 solution [67,68]. Another notable peak is the one related to water molecules that do not form hydrogen bonds, which is located around 3650 cm^{-1}. Interestingly, after the addition of the salt, O-H water band presents only one peak centered at 3550 cm^{-1}, meaning that there is a large contribution of non-bonding water. This phenomenon can be attributed to the strict bond formation between water molecules and ions through electrostatic forces, thereby precluding the possibility of hydrogen bond formation with other solvent molecules. Nevertheless, the center of the band is not exactly on the non-bonding water, suggesting that water molecules still make hydrogen bonds, which can be both with DMSO or other molecules, even if in significantly lower amounts.

As previously outlined, the two sharp peaks observed at 2900 and 3000 cm^{-1} correspond to the asymmetric and symmetric stretching, respectively, of the C-H bonds of DMSO. Upon the addition of water to DMSO, a shift in the peaks to higher wavenumbers is observed. This shift can be attributed to the formation of a specific hydrogen bond between

the methyl groups of DMSO and water, referred to as an "improper hydrogen bond". This interaction involves the transfer of electron density from one of the lone pairs of the oxygen atom in water to the hydrogen of the C-H bond in DMSO. However, the additional electron density does not remain on the methyl group, but is attracted towards the more electronegative $S = O$ bond, leading to a structural reorganization of the molecule. This reorganization results in a strengthening and shortening of the C-H bond, causing the observed blue shift [64,69]. In contrast to the conventional hydrogen bonds, where two strongly electronegative atoms are directly involved, the improper hydrogen bond allows for electron density movement, thus exhibiting a distinct characteristic. The addition of the salt enhances this shift, indicating that improper hydrogen bonds also arise from the interaction of DMSO with the electronegative groups of the FSI^- anion.

The ESW of the electrolytes was testedusing LSV (Fig. 5a). To assess practical applicability, three current collectors were tested: aluminum (Al), carbon-coated aluminum (CC-Al), and stainless steel (SS). Based on the results (Fig. S8, Supporting Information), Al and CC-Al provided the best performance in cathodic and anodic scanning modes, respectively. It should be pointed out that LiFSI is known to promote aluminum

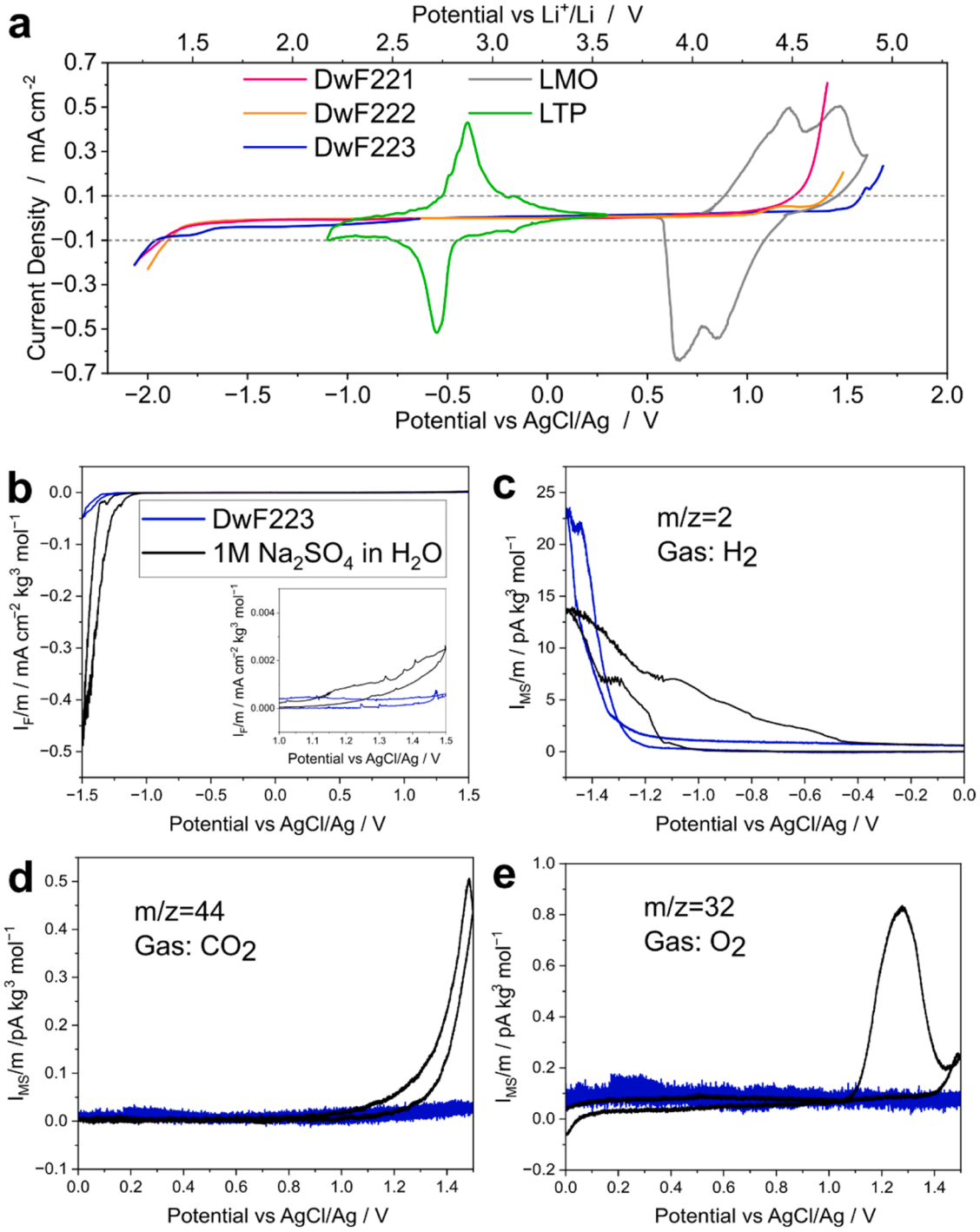

Fig. 5. Electrochemical stability of the electrolytes: (a) electrochemical stability windows of the electrolytes and lithiation/delithiation profiles of $LiTi_2(PO_4)_3$ and $LiMn_2O_4$; (b-e) DEMS results: (b) comparison between the normalized (with respect to water molality) ion currents of the standard diluted electrolyte and the DwF223 sample; (c) H_2 evolution; (d) CO_2 evolution; (e) O_2 evolution.

corrosion at high potentials [70], a phenomenon which is completely suppressed in the coated current collector.

On the negative side, all electrolytes exhibited similar stability, reaching approximately −2 V vs. AgCl/Ag. However, on the positive side, stability improved with increasing salt concentration, from 1.23 V vs. AgCl/Ag for DwF221 to 1.57 V for DwF223 (Table 3). As a result, the most concentrated electrolyte achieved an ESW exceeding 3.5 V, attributed to strong intermolecular interactions between water, LiFSI, and DMSO, which reduce water's availability for decomposition.

Typically, achieving such a wide ESW requires titanium as a current collector due to the corrosive nature of concentrated aqueous solutions [71]. However, titanium is expensive, dense, and classified as a critical raw material [72]. Demonstrating a 3.5 V ESW with Al-based collectors is a notable achievement that enhances the practical viability of these electrolytes.

To delve deeper into the stability of this class of electrolytes, differential electrochemical mass spectrometry (DEMS) was performed on DwF223, and the results were compared to those obtained with a standard 1 M solution of Na_2SO_4 in water. Please note that for the DEMS measurements a sputtered Ti was used as a current collector, which has a sufficient electrochemical stability at low and high potentials, thus allowing for the cyclic voltammetry measurements over the wide potential range of WISE. This setup was chosen and built starting from the results obtained in a previous work on water-based electrolytes [33]. The DEMS results are reported in Fig. 5b, c, d and e, Fig. S9, and Fig. S10, where the ion currents related to a series of gas products (H_2, CO_2, HF, SO_2 and O_2) on different current collectors (carbon-coated titanium for Figs. 5 and S9 and pure titanium for Fig. S10). As clearly observed from Figs. S9 and S10, the hybrid superconcentrated electrolyte shows a substantially lower gas evolution compared to the diluted water-based one. This trend is not only due to the different water content of the two electrolytes because it also clearly maintains when the relative amount of water is taken into consideration. Indeed, in Fig. 5c, d and e, the currents proportional to the evolution of H_2, CO_2, and O_2 are normalized by the water molality (10.4 mol kg^{-1} for DwF223, 55.5 mol kg^{-1} for the diluted solution). In particular, it can be seen that H_2 starts to evolve at a less negative potential for the 1 M Na_2SO_4 solution in water (below −1.2 V vs AgCl/Ag compared to the −0.6 V for the diluted solution), meaning that the hybrid superconcentrated electrolyte is significantly more stable towards reduction. Moreover, on the oxidation side, no gas evolution is present for the DwF223 electrolyte, where both oxygen and carbon dioxide evolve for the diluted solution, once again proving the high stability of the solution compared to a diluted water-based electrode. It is also noteworthy that HF, SO_2 (and many other possible gases) were also monitored by the mass spectrometer, but remained featureless at the background level over the entire potential range, indicating the absence of these possible products, as also shown in Figs. S9 and S10.

Given the proven stability of DwF223 electrolyte, to evaluate its potential applicability, lithium-ion full-cells were assembled using lithium-ion intercalation electrodes. The spinel $LiMn_2O_4$ (LMO) cathode and NASICON-type $LiTi_2(PO_4)_3$ (LTP) anode were selected due to their de-/lithiation potential being within the electrolyte ESW (Fig. 5a) and their suitability with water-based systems [73,74]. While the LTP negative electrode operates above the electrolyte's cathodic decomposition limit, future work could explore electrodes that intercalate lithium at ~−1 V vs. LTP. On the opposite side, the positive limit doesn't allow the use of higher energy materials suitable for water-based electrolytes, such as $LiNi_{0.5}Mn_{1.5}O_4$ [22,75], making LMO the perfect option available. However, this study primarily focuses on electrolyte electrochemical and physicochemical properties.

The CV profile of LTP displays a single reversible redox peak corresponding to Ti^{4+}/Ti^{3+} reduction and lithium insertion:

$$LiTi_2^{4+}(PO_4)_3 + 2Li^+ + 2e^- = Li_3Ti_2^{3+}(PO_4)_3$$

occurring between −0.56 V and −0.40 V vs. AgCl/Ag. In contrast, $LiMn_2O_4$ exhibits two redox processes corresponding to the lithium insertion/extraction from tetrahedral sites and the Mn^{4+}/Mn^{3+} redox transition [76].

$$LiMn^{3+}Mn^{4+}O_4 = Mn_2^{4+}O_4 + Li^+ + e^-$$

The Al/LTP/DwF223/LMO/CC-Al cell was cycled galvanostatically at 30 °C (Fig. 6a,b) and −10 °C (Fig. 6c,d). The 30 °C cell was cycled for 100 cycles between 0.9 V (discharge) and 2.1 V (charge) at 0.5C relative to the LTP mass. The first cycle exhibited significant irreversibility, with a coulombic efficiency of 45.3 %. However, efficiency improved to 99.5 % in subsequent cycles, achieving a specific capacity of 70 mAh g^{-1} (based on LTP mass) with 87 % retention after 100 cycles. The discharge potential remained stable at 1.5 V. Overall, the cell delivered an average specific energy of ~40 Wh/kg (sum of active material masses) with a round-trip efficiency decreasing from 89 % to 86 % over cycling.

Despite the optimization of the full cell setup is out of the scope of this work, some considerations may be made on the electrochemical performance. Considering the ESW of the hybrid electrolyte DwF223 and the operative potential of LMO, it is safe to assume that part of the inefficiency, particularly during the first cycle, is due to the formation of a Cathode Electrolyte Interphase (CEI). This is not in contrast to the DEMS measurements, as it is known that the stability window is not a hard thermodynamic limit, but rather a soft kinetic one which ultimately may depend on the nature of the electrode [77]. Such layer may remain stable or break with the volume changes on the cathode, and the stability depends on the nature of the electrolyte and its interaction with the cathode [78]. Other possible sources of irreversibility and capacity fading in water-containing electrolytes can be proton intercalation in the electrodes [79–81]. or reaction with dissolved species (like O_2) [82]. In all these cases, the optimization of cell performance must necessarily pass through the optimization of the type of electrodes used and their nature, which goes beyond the scope of this work, mainly focused on the electrolytes.

Water and DMSO form low-melting-point solutions, enabling low-temperature battery operation. Cycling was performed at −10 °C, the lowest temperature at which electrolyte conductivity remains above 10^{-4} S cm^{-1}, which is considered the threshold value of conductivity that an electrolyte must have for work in lithium-ion batteries [1]. To facilitate the operation of a battery with a less conductive electrolyte, it was decided to also lower the C-rate, passing from 0.5 C to 0.2 C, while the galvanic chain and the potential range are the same as the room temperature (RT) cycling measurement, i.e. between 2.1 and 0.9 V.

At −10 °C, the average specific capacity was approximately half that of the RT cell, decreasing from 36 mAh g_{LTP}^{-1} in the first cycle to 26 by the 50th cycle. The cell maintained a mean coulombic efficiency of 98.5 %, with a discharge capacity retention of 80.6 % after 50 cycles. The average discharge potential was 1.3 V, delivering a specific energy of about 15 Wh kg_{AM}^{-1} and a round-trip efficiency of 75 %.

The worsening of the cell performance when temperature decreases to −10 °C can be explained by the drastic increase in the electrolyte resistance, as observed in Fig. S11, with an increase of more than an order of magnitude. Another important effect to be taken into consideration is the increase in charge transfer resistance, in particular that of LMO.

Table 3
Electrochemical stability limit of the electrolytes.

Electrolyte	Negative side (on Al) / V vs AgCl/Ag	Positive side (on CC-Al) / V vs AgCl/Ag	Negative side (on Al) / V vs Li^+/Li	Positive side (on CC-Al) / V vs Li^+/Li	ESW / V
DwF221	−1.93	1.23	1.35	4.51	3.16
DwF222	−1.90	1.41	1.38	4.69	3.31
DwF223	−1.95	1.57	1.33	4.85	3.52

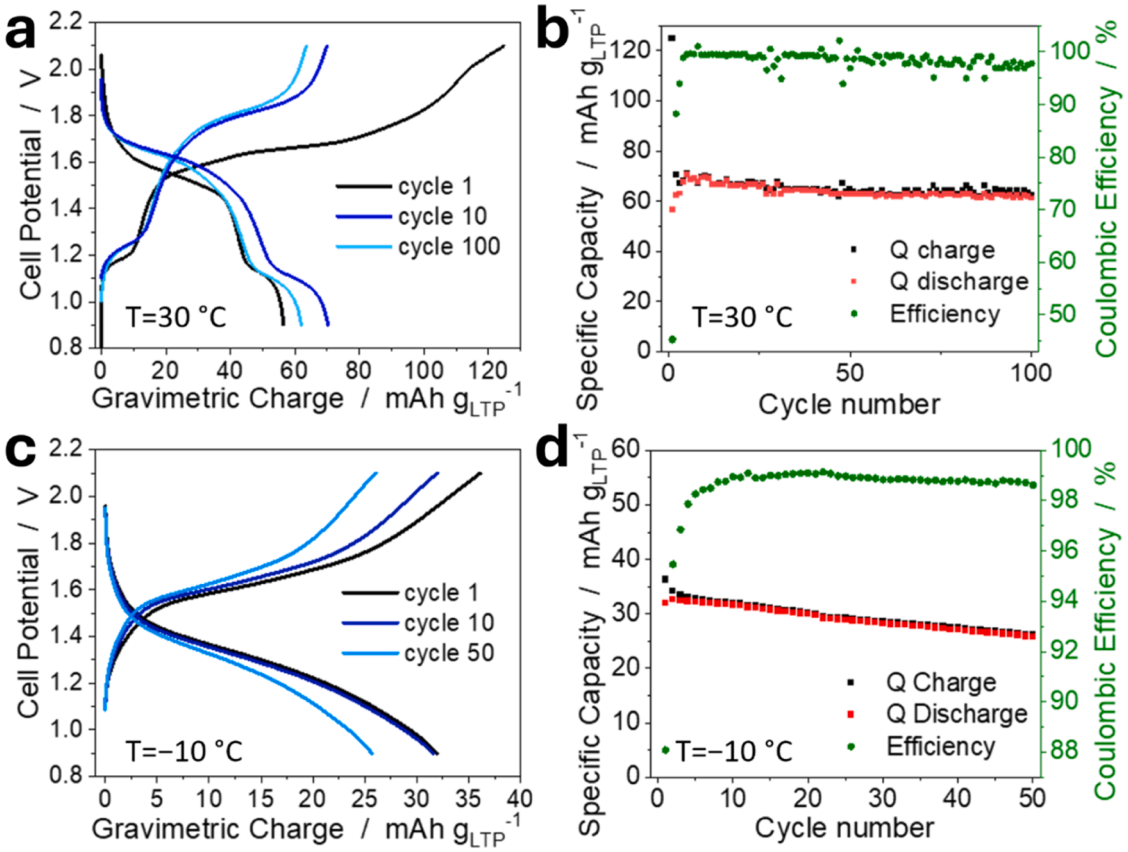

Fig. 6. Electrochemical characterizations of the electrolytes: (a) cycling curves of the LTP|DwF223|LMO full cell at room temperature; (b) capacity and efficiency trends of the LTP|DwF223|LMO cell at room temperature; (c) cycling curves of the LTP|DwF223|LMO cell at −10 °C; (d) capacity and efficiency trends of the LTP|DwF223|LMO cell at −10 °C.

Overheating tests were conducted on LMO/LTP coin cells using the ES-ARC technique, comparing the DwF223 electrolyte with commercial LP30 as a reference. These tests measured the maximum self-heating rate (SHR_{Max}) and the exothermal onset temperature (T_{exo}), which indicate thermal decomposition and potential thermal runaway [83,84].

Fig. 7 presents the temperature vs. time profiles for the charged cells. Both cells exhibited an initial degradation event around 180 °C, likely attributed to the positive electrode, as similar behaviour was observed in LMO-based cells with $Li_4Ti_5O_{12}$ anodes [21]. Given the superior thermal stability of NASICON structures compared to oxides, the degradation is primarily linked to the cathode.

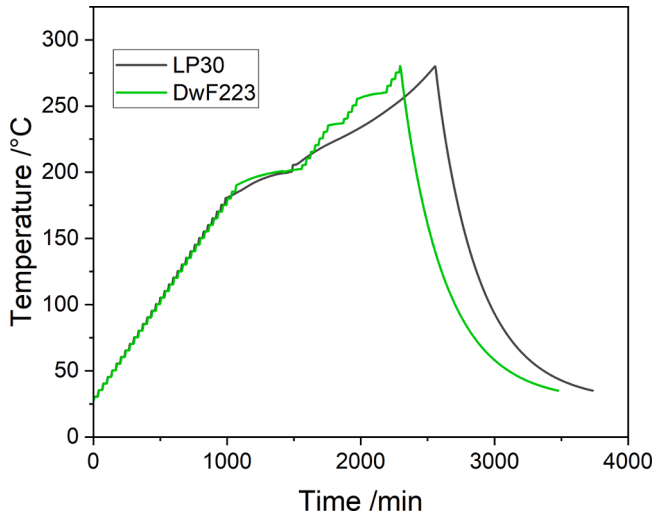

Fig. 7. Thermal runaway behaviour of the LTP|electrolyte|LMO cells at full charge using D2w2F3 and LP30 as electrolytes.

Beyond 180 °C, the DwF223 cell demonstrated enhanced thermal stability. A second degradation event occurred at 235 °C, though it was minor in terms of both self-heating and duration. A final event at 256 °C remained localized, allowing the cell to reach the imposed upper temperature limit of 280 °C without triggering thermal runaway.

In contrast, the LP30 cell exhibited two major exothermic events, with the second one occurring at 206 °C, ultimately leading to a thermal runaway. The superior stability of DwF223 was further confirmed by its lower SHR_{Max} value (0.065 °C min^{-1}) compared to LP30 (0.141 °C min^{-1}), indicating greater resistance to thermal abuse [85].

4. Conclusions

In this work, we propose dimethyl sulfoxide, DMSO, as a possible co-solvent for safe aqueous lithium-ion batteries. DMSO presents several advantages, such as great miscibility with water, cheapness and very low flammability. By adding the high soluble and largely employed salt lithium bis(fluorosulfonylimide), LiFSI, in different concentrations, three different electrolytes were prepared and fully characterized. The electrolytes resulted to be highly stable, both electrochemically, proving an electrochemical stability window up to 3.5 V (without use titanium current collectors), and thermally, without presenting any crystallization phenomenon, but only glass transitions lower than −70 °C. DEMS analyses confirmed that the high stability window of these hybrid electrolytes is accompanied by a clear decrease in the evolving gases, and above all by a shift of the onset of these evolutions to more extreme potentials when compared to diluted electrolyte.

PFG-NMR measurements reveal a clear deceleration in species diffusivity with increasing salt concentration, driven by rising viscosity and ion interactions. Water remains the most mobile component, while similar diffusion rates for Li^+, DMSO, and FSI^- suggest persistent coordination. Notably, Li^+ surpasses DMSO in mobility at high concentrations, indicating a shift toward a hopping conduction mechanism. This behavior is supported by transference number trends, reduced hydrodynamic radii, and relaxation data, all pointing to dynamic ligand exchange and increased contact ion pairing in concentrated electrolytes.

Moreover, we managed to explain the intermolecular interactions which allow such stability through Raman spectroscopy: water and DMSO make strong intermolecular bonds, able to generate low freezing point solutions and the salt addition can accentuate this outcome.

Based on the physicochemical information gathered on the three solutions in exam, the highest concentrated solution emerges as the best compromise between electrochemical stability and transport properties. In fact, the lower conductivity, probably due to an increase in viscosity, is at least partially compensated by an increase in the apparent lithium transference number.

Finally, we evaluate the full-cell performance by coupling the electrolytes with the two standard electrodes $LiTi_2(PO_4)_3$ and $LiMn_2O_4$ in a coin cell. The cell with the most concentrated electrolyte worked for 100 cycles with a C-rate of 0.5C delivering an average discharge potential of 1.5 V and a mean capacity of 60 mAh g_{LTP}^{-1}, which translates into an average energy of 40 Wh kg_{AM}^{-1}. In addition, we also performed a low-temperature cycling, which gave worse performances than the room temperature ones, but the differences are not so drastic, suggesting that the use of water/DMSO solutions could be a viable route for the development of energy storage devices working at low temperatures.

CRediT authorship contribution statement

Ivan Claudio Pellini: Writing – review & editing, Writing – original draft, Visualization, Validation, Methodology, Investigation, Data curation, Conceptualization. **Nicolò Pianta:** Writing – review & editing, Writing – original draft, Visualization, Data curation. **Daniele Callegari:** Writing – original draft, Visualization, Investigation, Data curation. **Gualtiero Conte:** Validation, Investigation. **Roberto Lorenzi:** Writing – original draft, Visualization, Methodology, Investigation. **Cataldo Simari:** Writing – original draft, Visualization, Investigation, Data curation. **Martina De Bonis:** Writing – original draft, Visualization, Investigation. **Silvia Leonardi:** Supervision, Resources, Funding acquisition. **Zenonas Jusys:** Data curation, Investigation, Methodology, Visualization. **Julio César Espinosa-Angeles:** Project administration, Supervision, Writing – review & editing. **Dominic Bresser:** Project administration, Resources, Supervision, Writing – review & editing. **Piercarlo Mustarelli:** Supervision, Resources, Funding acquisition, Conceptualization. **Riccardo Ruffo:** Writing – review & editing, Writing – original draft, Supervision, Resources, Project administration, Methodology, Funding acquisition, Conceptualization.

Declaration of competing interest

The authors declare the following financial interests/personal relationships which may be considered as potential competing interests:

Riccardo Ruffo reports financial support was provided by Eni SpA. Riccardo Ruffo reports a relationship with Eni SpA that includes: consulting or advisory and funding grants. If there are other authors, they declare that they have no known competing financial interests or personal relationships that could have appeared to influence the work reported in this paper.

Acknowledgements

This work was realized thanks to the MOST - Sustainable Mobility Center and received funding from the European Union Next Generation EU (PIANO NAZIONALE DI RIPRESA E RESILIENZA (PNRR) Missione 4 Componente 2, Investimento 1.4 DD. 1033 17/06/2022, CN00000023).

This study was carried out within the EnabLi project – funded by the Ministero dell'Università e della Ricerca – within the PRIN 2022 (program D.D.104–02/02/2022).

This work has been financed by Ministry of University and Research (MIUR) through grant "Dipartimenti di Eccellenza - 2017 "Materials for Energy", and by ENI Spa, under the Joint Research Agreement ENI-University of Milano Bicocca, grant number 5210001818.

Authors are grateful to the Program PE NEST - Network 4 Energy Sustainable Transition (code PE00000021 – CUP E13C22001890001) - PIANO NAZIONALE DI RIPRESA E RESILIENZA (PNRR) - MISSIONE 4 COMPONENTE 2 INVESTIMENTO 1.3 – funded by the European Union - NextGenerationEU – Bando a Cascata SUBAQUA

C.S. acknowledges financial support from "ORgANics for Green Electrochemical Energy Storage Project (ORANGEES)" funded by MASE "PT 2019–2021, DD 27.10.2021 bando a, DD 05.08.2022". This manuscript reflects only the authors' views and opinions, neither the European Union nor the European Commission can be considered responsible for them.

Z. Jusys, J.C. Espinosa-Angeles, and D. Bresser would like to acknowledge financial support from the Helmholtz Association. Moreover, I.C. Pellini would like to thank and highlight the practical contribution of Dr. Alberto Varzi, realizing the DEMS set-up utilised in this work.

Supplementary materials

Supplementary material associated with this article can be found, in the online version, at doi:10.1016/j.electacta.2025.146903.

Data availability

Data will be made available on request.

References

[1] J.B. Goodenough, Y. Kim, Challenges for rechargeable Li batteries, Chem. Mater. 22 (2010) 587–603, https://doi.org/10.1021/cm901452z.
[2] D. Larcher, J.M. Tarascon, Towards greener and more sustainable batteries for electrical energy storage, Nat. Chem. 7 (1 7) (2014) 19–29, https://doi.org/10.1038/nchem.2085, 2014.
[3] Y. Feng, L. Zhou, H. Ma, Z. Wu, Q. Zhao, H. Li, K. Zhang, J. Chen, Challenges and advances in wide-temperature rechargeable lithium batteries, Energy Environ. Sci. 15 (2022) 1711–1759, https://doi.org/10.1039/D1EE03292E.
[4] D. Doughty, E.P. Roth, A general discussion of Li ion battery safety, Electrochem. Society Interf. 21 (2012) 37–44, https://doi.org/10.1149/2.F03122IF/XML.
[5] C. Ferrara, R. Ruffo, E. Quartarone, P. Mustarelli, Circular economy and the fate of lithium batteries: second life and recycling, Adv. Energy Sustain. Res. 2 (2021) 2100047, https://doi.org/10.1002/AESR.202100047.
[6] L. Chen, L. Cao, X. Ji, S. Hou, Q. Li, J. Chen, C. Yang, N. Eidson, C. Wang, Enabling safe aqueous lithium ion open batteries by suppressing oxygen reduction reaction, Nat. Commun. 11 (1 11) (2020) 1–8, https://doi.org/10.1038/s41467-020-16460-w, 2020.
[7] L. Suo, O. Borodin, T. Gao, M. Olguin, J. Ho, X. Fan, C. Luo, C. Wang, K. Xu, Water-in-salt" electrolyte enables high-voltage aqueous lithium-ion chemistries, Science 350 (2015) (1979) 938–943, https://doi.org/10.1126/SCIENCE.AAB1595/SUPPL_FILE/SUO.SM.PDF.
[8] M. Li, C. Wang, Z. Chen, K. Xu, J. Lu, New concepts in electrolytes, Chem. Rev. 120 (2020) 6783–6819, https://doi.org/10.1021/ACS.CHEMREV.9B00531.
[9] D. Chao, W. Zhou, F. Xie, C. Ye, H. Li, M. Jaroniec, S.Z. Qiao, Roadmap for advanced aqueous batteries: from design of materials to applications, Sci. Adv. 6 (2020), https://doi.org/10.1126/SCIADV.ABA4098.
[10] S. Khalid, N. Pianta, P. Mustarelli, R. Ruffo, Use of water-In-salt concentrated liquid electrolytes in electrochemical energy storage: state of the art and perspectives, Batteries 9 (2023), https://doi.org/10.3390/batteries9010047.
[11] L. Suo, D. Oh, Y. Lin, Z. Zhuo, O. Borodin, T. Gao, F. Wang, A. Kushima, Z. Wang, H.C. Kim, Y. Qi, W. Yang, F. Pan, J. Li, K. Xu, C. Wang, How solid-electrolyte interphase forms in aqueous electrolytes, J. Am. Chem. Soc. 139 (2017) 18670–18680, https://doi.org/10.1021/JACS.7B10688/ASSET/IMAGES/JA-2017-10688N_M007.GIF.
[12] L. Suo, O. Borodin, W. Sun, X. Fan, C. Yang, F. Wang, T. Gao, Z. Ma, M. Schroeder, A. vonCresce, S.M. Russell, M. Armand, A. Angell, K. Xu, C. Wang, Advanced high-voltage aqueous lithium-ion battery enabled by "water-in-bisalt" electrolyte,

Angew. Chem. 128 (2016) 7252–7257, https://doi.org/10.1002/ANGE.201602397.
[13] S. Perez Beltran, P.B. Balbuena, SEI formation mechanisms and Li+ dissolution in lithium metal anodes: impact of the electrolyte composition and the electrolyte-to-anode ratio, J. Power Sources 551 (2022) 232203, https://doi.org/10.1016/J.JPOWSOUR.2022.232203.
[14] M. Wang, L. Huai, G. Hu, S. Yang, F. Ren, S. Wang, Z. Zhang, Z. Chen, Z. Peng, C. Shen, D. Wang, Effect of LiFSI concentrations to form thickness- and modulus-controlled SEI layers on lithium metal anodes, J. Phys. Chem. C 122 (2018) 9825–9834, https://doi.org/10.1021/ACS.JPCC.8B02314/SUPPL_FILE/JP8B02314_SI_001.PDF.
[15] Y. Chen, J. Fan, Q. Li, P. Yi, H. Tu, D. Shan, W. Wang, S. Zhao, Y. Zhang, Y. Wu, Y. Chen, D. Xiao, Sacrificial reduction effects derived inorganic-rich hybrid solid electrolyte interfaces for long-term and high reversibility aqueous zinc-ion batteries, Chem. Eng. J. 510 (2025) 161858, https://doi.org/10.1016/J.CEJ.2025.161858.
[16] L. Chen, J. Zhang, Q. Li, J. Vatamanu, X. Ji, T.P. Pollard, C. Cui, S. Hou, J. Chen, C. Yang, L. Ma, M.S. Ding, M. Garaga, S. Greenbaum, H.S. Lee, O. Borodin, K. Xu, C. Wang, A 63 m superconcentrated aqueous electrolyte for high-energy Li-ion batteries, ACS Energy Lett. 5 (2020) 968–974, https://doi.org/10.1021/ACSENERGYLETT.0C00348/ASSET/IMAGES/LARGE/NZ0C00348_0004.JPEG.
[17] R. Li, G.Shen /Eesbatteries, S. Kondou, G. Wada, H. Nakagaki, M. Watanabe, K. Dokko, K. Ueno, Interfacially-localized high-concentration electrolytes for high-performance rechargeable aqueous lithium-ion batteries, EES Batteries 1 (2025) 273–286, https://doi.org/10.1039/D4EB00036F.
[18] L. Wang, A. Menakath, F. Han, Y. Wang, P.Y. Zavalij, K.J. Gaskell, O. Borodin, D. Iuga, S.P. Brown, C. Wang, K. Xu, B.W. Eichhorn, Identifying the components of the solid–electrolyte interphase in Li-ion batteries, Nat. Chem. 11 (2019) 789–796, https://doi.org/10.1038/s41557-019-0304-z.
[19] J. Vatamanu, O. Borodin, Ramifications of water-in-salt interfacial structure at charged electrodes for electrolyte electrochemical stability, J. Phys. Chem. Lett. 8 (2017) 4362–4367, https://doi.org/10.1021/ACS.JPCLETT.7B01879.
[20] J. Chen, J. Vatamanu, L. Xing, O. Borodin, H. Chen, X. Guan, X. Liu, K. Xu, W. Li, Improving electrochemical stability and low-temperature performance with water/acetonitrile hybrid electrolytes, Adv. Energy Mater. 10 (2020) 1902654, https://doi.org/10.1002/AENM.201902654.
[21] S. Khalid, I.C. Pellini, N. Pianta, R. Lorenzi, S. Leonardi, L. Meda, C. Rizzo, E. Roccaro, P. Johansson, P. Mustarelli, R. Ruffo, Stable lithium-ion batteries based on a hybrid aqueous/organic electrolyte, J. Power Sources 612 (2024) 234803, https://doi.org/10.1016/J.JPOWSOUR.2024.234803.
[22] F. Wang, O. Borodin, M.S. Ding, M. Gobet, J. Vatamanu, X. Fan, T. Gao, N. Edison, Y. Liang, W. Sun, S. Greenbaum, K. Xu, C. Wang, Hybrid aqueous/non-aqueous electrolyte for safe and high-energy Li-ion batteries, Joule 2 (2018) 927–937, https://doi.org/10.1016/j.joule.2018.02.011.
[23] 陆雅翔陈立泉 Q. Guo, S. 郭秋卜, 韩.帅. Han, Y. Lu, L. Chen, Y.-S. Hu, 胡勇胜, low-temperature aqueous Na-ion batteries: strategies and challenges of electrolyte design, Chinese Phys. Lett. 40 (2023) 028801 https://doi.org/10.1088/0256-307X/40/2/028801.
[24] J. Xie, Z. Liang, Y.C. Lu, Molecular crowding electrolytes for high-voltage aqueous batteries, Nat. Mater. 19 (9 19) (2020) 1006–1011, https://doi.org/10.1038/s41563-020-0667-y, 2020.
[25] J.T. Yik, C. Hvarfner, J. Sjölund, E.J. Berg, L. Zhang, Accelerating aqueous electrolyte design with automated full-cell battery experimentation and Bayesian optimization, Cell Rep. Phys. Sci. 6 (2025) 102548, https://doi.org/10.1016/j.xcrp.2025.102548.
[26] Merck Life Science S.r.l., Dimethyl sulfoxide SAFETY DATA SHEET according to regulation (EC) No. 1907/2006, 2020.
[27] Q. Nian, J. Wang, S. Liu, T. Sun, S. Zheng, Y. Zhang, Z. Tao, J. Chen, Aqueous batteries operated at −50 °C, Angew. Chem. 131 (2019) 17150–17155, https://doi.org/10.1002/ange.201908913.
[28] C.F. Brayton, Dimethyl sulfoxide (DMSO): a review, Cornell. Vet. 76 (1986) 61–90. https://europepmc.org/article/med/3510103. accessed July 9, 2024.
[29] R.N. Havemeyer, Freezing point curve of dimethyl sulfoxide—Water solutions, J. Pharm. Sci. 55 (1966) 851–853, https://doi.org/10.1002/jps.2600550822.
[30] M. Tribbia, N. Pianta, G. Brugnetti, R. Lorenzi, R. Ruffo, A new double layer supercapacitor made by free-standing activated carbon membranes and highly concentrated potassium acetate solutions, Electrochim. Acta 364 (2020) 137323, https://doi.org/10.1016/J.ELECTACTA.2020.137323.
[31] E.O. Stejskal, J.E. Tanner, Spin diffusion measurements: spin echoes in the presence of a time-dependent field gradient, J. Chem. Phys. 42 (1965) 288–292, https://doi.org/10.1063/1.1695690.
[32] Z. Jusys, M. Binder, J. Schnaidt, R.J. Behm, A novel DEMS approach for studying gas evolution at battery-type electrode|electrolyte interfaces: high-voltage LiNi0.5Mn1.5O4 cathode in ethylene and dimethyl carbonate electrolytes, Electrochim Acta 314 (2019) 188–201, https://doi.org/10.1016/J.ELECTACTA.2019.05.076.
[33] H. Fei, F. Yang, Z. Jusys, S. Passerini, A. Varzi, Ethylene glycol Co-solvent enables stable aqueous ammonium-ion batteries with diluted electrolyte, Adv. Funct. Mater. 34 (2024) 2404560, https://doi.org/10.1002/ADFM.202404560.
[34] M. Hilder, M. Gras, C.R. Pope, M. Kar, D.R. Macfarlane, M. Forsyth, L.A. O'Dell, Effect of mixed anions on the physicochemical properties of a sodium containing alkoxyammonium ionic liquid electrolyte, Phys. Chem. Chem. Phys. 19 (2017) 17461–17468, https://doi.org/10.1039/c7cp03318d.
[35] L. Herbers, V. Küpers, M. Winter, P. Bieker, An ionic liquid- and PEO-based ternary polymer electrolyte for lithium metal batteries: an advanced processing solvent-free approach for solid electrolyte processing, RSC Adv 13 (2023) 17947–17958, https://doi.org/10.1039/D3RA02488A.
[36] B. Ravikumar, M. Mynam, S. Repaka, B. Rai, Solvation shell dynamics explains charge transport characteristics of LIB electrolytes, J Mol Liq 338 (2021) 116613, https://doi.org/10.1016/J.MOLLIQ.2021.116613.
[37] C.A. Angell, K.L. Ngai, G.B. McKenna, P.F. McMillan, S.W. Martin, Relaxation in glassforming liquids and amorphous solids, J. Appl. Phys. 88 (2000) 3113–3157, https://doi.org/10.1063/1.1286035.
[38] W.V. Barth, A. Peña Hueso, L. Zhou, L.J. Lyons, R. West, Ionic conductivity studies of LiBOB-doped silyl solvent blend electrolytes for lithium-ion battery applications, J. Power Sources 272 (2014) 190–195, https://doi.org/10.1016/J.JPOWSOUR.2014.08.075.
[39] L. Mezzomo, N. Pianta, I. Ostroman, N. Aloni, D. Golodnitsky, E. Peled, P. Mustarelli, R. Ruffo, Deep eutectic solvent electrolytes based on trifluoroacetamide and LiPF6 for Li-metal batteries, J. Power Sources 561 (2023) 232746, https://doi.org/10.1016/J.JPOWSOUR.2023.232746.
[40] M.S. Ding, Q. Li, X. Li, W. Xu, K. Xu, Effects of solvent composition on liquid range, glass transition, and conductivity of electrolytes of a (Li, Cs)PF6 salt in EC-PC-EMC solvents, J. Phys. Chem. C 121 (2017) 11178–11183, https://doi.org/10.1021/ACS.JPCC.7B03306/ASSET/IMAGES/LARGE/JP-2017-03306X_0006.JPEG.
[41] M.S. Ding, A. Von Cresce, K. Xu, Conductivity, viscosity, and their correlation of a super-concentrated aqueous electrolyte, J. Phys. Chem. C 121 (2017) 2149–2153, https://doi.org/10.1021/acs.jpcc.6b12636.
[42] M.S. Ding, K. Xu, T.R. Jow, Effects of tris(2,2,2-trifluoroethyl) phosphate as a flame-retarding cosolvent on physicochemical properties of electrolytes of LiPF [sub 6] in EC-PC-EMC of 3:3:4 weight ratios, J. Electrochem. Soc. 149 (2002) A1489, https://doi.org/10.1149/1.1513556/XML.
[43] Y. Wang, W. Chen, Q. Zhao, G. Jin, Z. Xue, Y. Wang, T. Mu, Ionicity of deep eutectic solvents by Walden plot and pulsed field gradient nuclear magnetic resonance (PFG-NMR), Phys. Chem. Chem. Phys. 22 (2020) 25760–25768, https://doi.org/10.1039/D0CP01431A.
[44] O. Borodin, L. Suo, M. Gobet, X. Ren, F. Wang, A. Faraone, J. Peng, M. Olguin, M. Schroeder, M.S. Ding, E. Gobrogge, A. Von Wald Cresce, S. Munoz, J.A. Dura, S. Greenbaum, C. Wang, K. Xu, Liquid structure with nano-heterogeneity promotes cationic transport in concentrated electrolytes, ACS Nano 11 (2017) 10462–10471, https://doi.org/10.1021/acsnano.7b05664.
[45] M. McEldrew, Z.A.H. Goodwin, A.A. Kornyshev, M.Z. Bazant, Theory of the double layer in water-in-salt electrolytes, J. Phys. Chem. Lett. 9 (2018) 5840–5846, https://doi.org/10.1021/acs.jpclett.8b02543.
[46] Anionic effects on the structure and dynamics of water in superconcentrated aqueous electrolytes _ enhanced reader, (n.d.).
[47] K. Dokko, D. Watanabe, Y. Ugata, M.L. Thomas, S. Tsuzuki, W. Shinoda, K. Hashimoto, K. Ueno, Y. Umebayashi, M. Watanabe, Direct evidence for Li ion hopping conduction in highly concentrated sulfolane-based liquid electrolytes, J. Phys. Chem. B 122 (2018) 10736–10745, https://doi.org/10.1021/ACS.JPCB.8B09439/SUPPL_FILE/JP8B09439_SI_004.CIF.
[48] J. Alvarado, M.A. Schroeder, M. Zhang, O. Borodin, E. Gobrogge, M. Olguin, M.S. Ding, M. Gobet, S. Greenbaum, Y.S. Meng, K. Xu, A. Carbonate-free, Sulfone-based electrolyte for high voltage Li-ion batteries, (2018).
[49] P.L. Stigliano, N. Pianta, S. Bonizzoni, M. Mauri, R. Simonutti, R. Lorenzi, B. Vigani, V. Berbenni, Si. Rossi, P. Mustarelli, R. Ruffo, A physico-chemical investigation of highly concentrated potassium acetate solutions towards applications in electrochemistry _ Enhanced Reader, Phys. Chem. Chem. Phys (2021).
[50] A. Nakanishi, K. Ueno, D. Watanabe, Y. Ugata, Y. Matsumae, J. Liu, M.L. Thomas, K. Dokko, M. Watanabe, Sulfolane-based highly concentrated electrolytes of lithium bis(trifluoromethanesulfonyl)amide: ionic transport, Li-ion coordination, and Li-S battery performance, J. Phys. Chem. C 123 (2019) 14229–14238, https://doi.org/10.1021/ACS.JPCC.9B02625/ASSET/IMAGES/LARGE/JP-2019-02625J_0011.JPEG.
[51] C. Zhang, A. Yamazaki, J. Murai, J.W. Park, T. Mandai, K. Ueno, K. Dokko, M. Watanabe, Chelate effects in glyme/lithium bis(trifluoromethanesulfonyl) amide solvate ionic liquids, part 2: importance of solvate-structure stability for electrolytes of lithium batteries, J. Phys. Chem. C 118 (2014) 17362–17373, https://doi.org/10.1021/JP504099Q/SUPPL_FILE/JP504099Q_SI_001.PDF.
[52] B.W. Zewde, L. Carbone, S. Greenbaum, J. Hassoun, A novel polymer electrolyte membrane for application in solid state lithium metal battery, Solid State Ion 317 (2018) 97–102, https://doi.org/10.1016/J.SSI.2017.12.039.
[53] V. Piacentini, C. Simari, E. Mangiacapre, A. Pierini, A. Gentile, S. Marchionna, I. Nicotera, S. Brutti, E. Bodo, Aprotic electrolytes beyond organic carbonates: transport properties of LiTFSI solutions in S-based solvents, ChemSusChem (2025) e202402273, https://doi.org/10.1002/CSSC.202402273.
[54] Y. Zhao, Z. Huang, S. Chen, B. Chen, J. Yang, Q. Zhang, F. Ding, Y. Chen, X. Xu, A promising PEO/LAGP hybrid electrolyte prepared by a simple method for all-solid-state lithium batteries, Solid State Ion 295 (2016) 65–71, https://doi.org/10.1016/J.SSI.2016.07.013.
[55] W. Gorecki, M. Jeannin, E. Belorizky, C. Roux, M. Armand, Physical properties of solid polymer electrolyte PEO(LiTFSI) complexes, J. Phys.: Conden. Matter. 7 (1995) 6823, https://doi.org/10.1088/0953-8984/7/34/007.
[56] K. Xu, Nonaqueous liquid electrolytes for lithium-based rechargeable batteries, Chem. Rev. 104 (2004) 4303–4417, https://doi.org/10.1021/CR030203G/ASSET/CR030203G.FP.PNG_V03.
[57] M. Takeuchi, Y. Kameda, Y. Umebayashi, S. Ogawa, T. Sonoda, S. ichi Ishiguro, M. Fujita, M. Sano, Ion–ion interactions of LiPF6 and LiBF4 in propylene carbonate solutions, J. Mol. Liq. 148 (2009) 99–108, https://doi.org/10.1016/J.MOLLIQ.2009.07.003.

[58] M. Okuno, Hyper-raman spectroscopy of polar liquids excited at 1064 nm: acetone, acetonitrile, chloroform, and dimethyl sulfoxide, J. Chem. Phys. 152 (2020) 174202, https://doi.org/10.1063/5.0004755/198306.
[59] K. Noack, J. Kiefer, A. Leipertz, Concentration-dependent hydrogen-bonding effects on the dimethyl sulfoxide vibrational structure in the presence of water, Methanol, Ethanol, ChemPhysChem 11 (2010) 630–637, https://doi.org/10.1002/CPHC.200900691.
[60] K. Matsumoto, T. Oka, T. Nohira, R. Hagiwara, Polymorphism of alkali bis (fluorosulfonyl)amides (M[N(SO2F) 2], M = Na, K, and Cs), Inorg. Chem. 52 (2013) 568–576, https://doi.org/10.1021/IC3010486/SUPPL_FILE/IC3010486_SI_002.PDF.
[61] Y. Yamada, K. Usui, C.H. Chiang, K. Kikuchi, K. Furukawa, A. Yamada, General observation of lithium intercalation into graphite in ethylene-carbonate-free superconcentrated electrolytes, ACS Appl. Mater. Interf. 6 (2014) 10892–10899, https://doi.org/10.1021/am5001163.
[62] S.-D. Han, R.D. Sommer, P.D. Boyle, Z.-B. Zhou, V.G. Young, O. Borodin, W. A. Henderson, Electrolyte Solvation and Ionic Association: part IX. Structures and raman spectroscopic characterization of LiFSI solvates, J. Electrochem. Soc. 169 (2022) 110544, https://doi.org/10.1149/1945-7111/AC9A07.
[63] M.I.S. Sastry, S. Singh, Self-association of dimethyl sulphoxide and its dipolar interactions with water: raman spectral studies, J. Raman Spectroscopy 15 (1984) 80–85, https://doi.org/10.1002/JRS.1250150203.
[64] S. Singh, S.K. Srivastava, D.K. Singh, Raman scattering and DFT calculations used for analyzing the structural features of DMSO in water and methanol, RSC Adv. 3 (2013) 4381–4390, https://doi.org/10.1039/C3RA22730H.
[65] S. Khalid, N. Pianta, S. Bonizzoni, C. Ferrara, R. Lorenzi, A. Paleari, P. Johansson, P. Mustarelli, R. Ruffo, Structure-property correlations in aqueous binary Na+/K+-CH3COO- highly concentrated electrolytes, J. Phys. Chem. C 127 (2023) 9823–9832, https://doi.org/10.1021/ACS.JPCC.3C01017/ASSET/IMAGES/LARGE/JP3C01017_0008.JPEG.
[66] D.M. Carey, G.M. Korenowski, Measurement of the Raman spectrum of liquid water, J. Chem. Phys. 108 (1998) 2669–2675, https://doi.org/10.1063/1.475659.
[67] B. Yang, X. Cao, C. Wang, S. Wang, C. Sun, Investigation of hydrogen bonding in water/DMSO binary mixtures by Raman spectroscopy, Spectrochim Acta A Mol. Biomol. Spectrosc. 228 (2020) 117704, https://doi.org/10.1016/J.SAA.2019.117704.
[68] I.A. Borin, M.S. Skaf, Molecular association between water and dimethyl sulfoxide in solution: a molecular dynamics simulation study, J. Chem. Phys. 110 (1999) 6412–6420, https://doi.org/10.1063/1.478544.
[69] P. Hobza, Z. Havlas, Blue-shifting hydrogen bonds, Chem. Rev. 100 (2000) 4253–4264, https://doi.org/10.1021/CR990050Q/ASSET/IMAGES/LARGE/CR990050QF00010.JPEG.
[70] A. Abouimrane, J. Ding, I.J. Davidson, Liquid electrolyte based on lithium bis-fluorosulfonyl imide salt: aluminum corrosion studies and lithium ion battery investigations, J. Power Sources 189 (2009) 693–696, https://doi.org/10.1016/J.JPOWSOUR.2008.08.077.
[71] J. Liu, C. Yang, X. Chi, B. Wen, W. Wang, Y. Liu, Water/sulfolane hybrid electrolyte achieves ultralow-temperature operation for high-voltage aqueous lithium-ion batteries, Adv. Funct. Mater. 32 (2022), https://doi.org/10.1002/ADFM.202106811.
[72] accessed July 22, EUR-lex - 52020DC0474 - EN - EUR-lex (n.d.), https://eur-lex.europa.eu/legal-content/EN/TXT/?uri=CELEX:52020DC0474, 2024.
[73] T. Xu, M. Zhao, Z. Su, W. Duan, Y. Shi, Z. Li, V.G. Pol, X. Song, Nanostructured LiTi2(PO4)3 anode with superior lithium and sodium storage capability aqueous electrolytes, J. Power Sources 481 (2021) 229110, https://doi.org/10.1016/J.JPOWSOUR.2020.229110.
[74] Y. Wen, C. Ma, H. Chen, H. Zhang, M. Li, P. Zhao, J. Qiu, H. Ming, G. Cao, G. Tang, Stabilizing LiMn2O4 cathode in aqueous electrolyte with optimal concentration and components, Electrochim. Acta 362 (2020) 137079, https://doi.org/10.1016/J.ELECTACTA.2020.137079.
[75] Z. Yao, T. Fu, T. Pan, C. Luo, M. Pang, S. Xiong, Q. Guo, Y. Li, S. Liu, C. Zheng, W. Sun, Dynamic doping and interphase stabilization for cobalt-free and high-voltage lithium metal batteries, Nat. Commun. 16 (1 16) (2025) 1–13, https://doi.org/10.1038/s41467-025-58110-z, 2025.
[76] T. Ohzuku, M. Kitagawa, T. Hirai, Electrochemistry of manganese dioxide in lithium nonaqueous cell: III . X-ray diffractional study on the reduction of spinel-related manganese dioxide, J. Electrochem. Soc. 137 (1990) 769–775, https://doi.org/10.1149/1.2086552/XML.
[77] P. Ruschhaupt, S. Pohlmann, A. Varzi, S. Passerini, Determining realistic electrochemical stability windows of electrolytes for electrical double-layer capacitors, Batter. Supercaps 3 (2020) 698–707, https://doi.org/10.1002/BATT.202000009.
[78] P. Jiang, J. Zhang, T. Zhan, K. Zhang, W. Jian, D. Ruan, Constructing a robust cathode electrolyte interface for aqueous hybrid lithium-ion batteries via regulating the solvent-solute interaction in a locally concentrated electrolyte, ACS Mater. Lett. 6 (2024) 1216–1223, https://doi.org/10.1021/ACSMATERIALSLETT.3C01478/SUPPL_FILE/TZ3C01478_SI_001.PDF.
[79] Y. Wang, J. Lou, W. Wu, C. Wang, Y. Xia, Hybrid aqueous energy storage cells using activated carbon and lithium-ion intercalated compounds: III. Capacity fading mechanism of at different pH electrolyte solutions, J. Electrochem. Soc. 154 (2007) A228, https://doi.org/10.1149/1.2432056.
[80] A.I. Mohamed, J.F. Whitacre, Capacity fade of NaTi2(PO4)3 in aqueous electrolyte solutions: relating pH increases to long term stability, Electrochim. Acta 235 (2017) 730–739, https://doi.org/10.1016/J.ELECTACTA.2017.03.106.
[81] F. Wang, L.E. Blanc, Q. Li, A. Faraone, X. Ji, H.H. Chen-Mayer, R.L. Paul, J.A. Dura, E. Hu, K. Xu, L.F. Nazar, C. Wang, Quantifying and suppressing proton intercalation to enable high-voltage Zn-ion batteries, Adv. Energy Mater. 11 (2021) 2102016, https://doi.org/10.1002/AENM.202102016.
[82] P. He, J.L. Liu, W.J. Cui, J.Y. Luo, Y.Y. Xia, Investigation on capacity fading of LiFePO4 in aqueous electrolyte, Electrochim. Acta 56 (2011) 2351–2357, https://doi.org/10.1016/J.ELECTACTA.2010.11.027.
[83] S. Ohneseit, P. Finster, C. Floras, N. Lubenau, N. Uhlmann, H.J. Seifert, C. Ziebert, Thermal and mechanical safety assessment of type 21700 lithium-ion batteries with NMC, NCA and LFP cathodes–Investigation of cell abuse by means of accelerating rate calorimetry (ARC), Batteries 9 (2023) 237, https://doi.org/10.3390/batteries9050237.
[84] A. Börger, J. Mertens, H. Wenzl, Thermal runaway and thermal runaway propagation in batteries: what do we talk about? J. Energy Storage 24 (2019) 100649 https://doi.org/10.1016/J.EST.2019.01.012.
[85] N. Mao, S. Gadkari, Z. Wang, T. Zhang, J. Bai, Q. Cai, A comparative analysis of lithium-ion batteries with different cathodes under overheating and nail penetration conditions, Energy 278 (2023) 128027, https://doi.org/10.1016/J.ENERGY.2023.128027.